*Progress In Electromagnetics Research, Vol. 172, 77–88, 2021*

# A Single-Layer Focusing Metasurface Based on Induced Magnetism

**Hong-Gang Hao, Xuehong Ran*, Yihao Tang, Sen Zheng, and Wei Ruan***

**Abstract**—A transmissive single-layer Huygens unit cell based on induced magnetism is proposed to design low-profile and multi-focus metasurface. The Huygens unit cell consists of a pair of antisymmetric metal elements and a dielectric substrate with only 1.2 mm thickness ($\lambda_0/6.8$ at 37 GHz). The surface currents flowing in the opposite directions form the circulating electric currents to induce the magnetic currents orthogonal to the electric currents. The full coverage of $2\pi$ phase is achieved through optimizing the parameters of the metal elements, which solves the problem of the incomplete phase coverage caused by layer number reduction. With Holographic theory, the compensating phase distribution on the metasurface is calculated. The incident plane wave can be converged to designated points in any desired fashion including focal number, location, and intensity distribution, which exhibits outstanding manipulation capability. As the simulations and measured results show, the designed metasurface can achieve good multi-focus focusing characteristics. The focusing efficiency at the center frequency is 43.78%, and the relative bandwidth with 20% focusing efficiency exceeds 20%. The designed metasurface has the advantages of low profile, simple processing, and high efficiency, which has a wide range of application prospects in the fields of millimeter wave imaging, biomedical diagnosis and detection.

## 1. INTRODUCTION

In an optical system, a refractive optical device is one of the most commonly used components, which can control the convergence and divergence of light. It is widely applied in the fields of detection [1, 2], imaging [3, 4], medical diagnosis [5, 6], and other fields [7–9], and has always been a research hotspot in academia and industry. The change of the wavefront of a beam is mainly caused by the cumulative phase of light passing through a medium over a distance. Consequently, In the millimeter wave and microwave bands, the sizes of the refractive optical elements are usually much larger than the light wavelength, which limits the optical device miniaturization. As a new kind of two-dimensional material that can be designed and manufactured, metasurface exhibits exotic properties beyond natural materials, which can flexibly control the amplitude [10, 11], phase [12, 13], and polarization [14, 15] of electromagnetic waves on the sub-wavelength scale, and offer an opportunity to greatly reduce the sizes of beam shaping elements.

Generally, the key characteristics of a transmission metasurface include phase shift, operating frequency, and transmission efficiency. However, it is difficult to generate a full phase range from 0 to $2\pi$ using only a single layer structure to effectively and accurately manipulate the incident wavefront. Therefore, multilayer stacking has been suggested to achieve high-performance metasurface. Despite its favorable characteristics, multilayer stacking methodology is not an optimal solution for developing compact and light weight microwave devices for mobile applications [16, 17]. In [18], a low-loss Huygens metasurface that could simultaneously control electric and magnetic currents was proposed, providing a systematic theoretical foundation to achieve the manipulation of transmission

*Received 16 November 2021, Accepted 28 December 2021, Scheduled 2 January 2022*
* Corresponding author: Xuehong Ran (s190402004@stu.cqupt.edu.cn), Wei Ruan (ruanwei@cqupt.edu.cn).
The authors are with the College of Electronic Engineering, Chongqing University of Posts and Telecommunications, Chongqing 400065, China.

and refection independently. The half-powered bandwidth and peak efficiency of the refracted beam are 24.2% and 86%, respectively. Due to the fascinating wave-manipulating ability of Huygens metasurface, various applications have been reported in beam-shaping [19, 20], focusing [21, 22], and antenna [23, 24]. In [20], a double-layer ultra-thin Huygens metasurface with vias was proposed, which greatly reduced the coupling between structures, providing full coverage of $2\pi$ transmission phase. The maximum efficiency of refracted beams was 60%. A reconfigurable Huygens metasurface [22] was designed to realize real-time adjustment of single and double focus on a non-planar structure by loading active devices, with the total focusing efficiency of approximately 36%. In [24], a curved conformal transmission Huygens metasurface was developed, which achieved $2\pi$ phase coverage by adjusting the electrical and magnetic polarization currents. The antenna efficiency was 47%, and the 3 dB gain bandwidth was 3.7%. However, there is a little study on the issue of focusing at several points in the near field region, especially in the millimeter wave band. Near field focusing metasurfaces are of interest in millimeter wave frequencies for a variety of applications such as remote sensing, medical targeting devices, internet of things, and wireless power transfer.

In this work, a Huygens unit cell is designed for focusing metasurface with multi-focus characteristics. The major feature of the design is that only two asymmetric electric dipole elements are used without a separate magnetic dipole component. It can induce virtual magnetic currents by electrical currents flowing in the opposite direction, orthogonal to electric currents, excitation electromagnetic resonance. Induced magnetism makes the magnetic element super-latticed instead of stacking a separate magnetic element in one lattice, thereby reducing the number of layers and no vias. Here, a dual-focus transmission metasurface with specific focal intensity ratio is designed, processed, and tested. Numerical simulation results of the proposed metasurface agree well with the theoretical ones, which adds a new degree of advantage to the manipulation of electromagnetic wave.

## 2. MATESURFACE UNIT CELL

The physical structure of the unit cell is directly related to the pros and cons of metasurface properties. For transmission metasurfaces, the unit cell needs to have high transmission amplitude and complete $2\pi$ phase coverage. The Huygens unit cell is composed of crossed magnetic and electric dipoles which can induce surface electric ($J_s$) and magnetic ($M_s$) currents under normal incidence to generate specific electromagnetic resonance. The electromagnetic resonance produced can manipulate the scattered electric and magnetic field distribution on both sides of the metasurface indirectly according to the boundary condition. The relationship between surface currents and electromagnetic field can be defined by surface electric admittance ($Y_{es}$) and magnetic impedance ($Z_{ms}$), which can be modified by changing the metal elements of unit cell appropriately. Then, based on the scattered field distribution, the relationship between the refection ($R$) and transmission ($T$) coefficients and the surface electric admittance and magnetic impedance can be built.

$$\begin{aligned} Y_{es} &= \frac{2\,(1-T-R)}{\eta\,(1+T+R)} \\ Z_{ms} &= \frac{2\eta\,(1-T+R)}{(1+T-R)} \end{aligned} \tag{1}$$

where $\eta$ is the wave impedance of free space. For the transmission Huygens metasurface, $R = 0$ and $T = 1$.

$$\begin{aligned} Y_{es} &= \frac{2}{j\eta}\frac{2-2\cos\varphi_t}{\sin\varphi_t} \\ Z_{ms} &= -j2\eta\frac{\sin\varphi_t}{2-2\cos\varphi_t} \end{aligned} \tag{2}$$

where $\varphi_t$ represents the transmission phase, which changes from 0 to $2\pi$. It can be seen from Eq. (2) that $Y_{es}$ and $Z_{ms}$ are pure imaginary numbers and are related to the transmission phase. Theoretically, if the normalized electric admittance and magnetic impedance are equal and pure imaginary numbers, the transmission amplitude reaches unity without reflection, and the electromagnetic resonance is achieved.

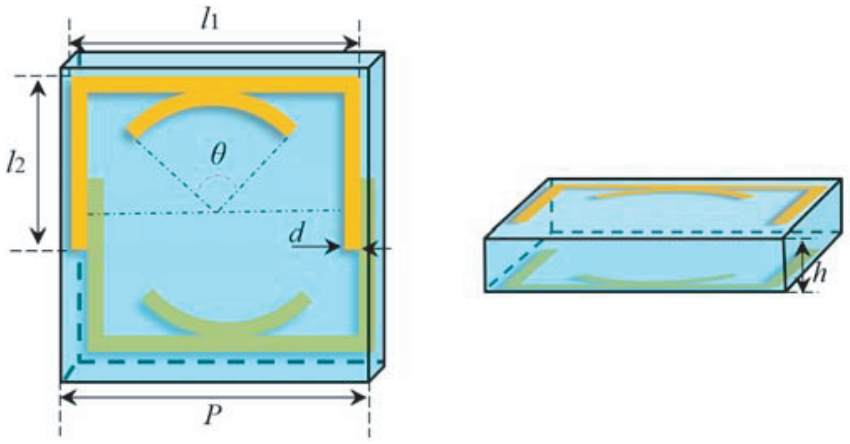


**Figure 1.** Structure of unit cell.

The designed Huygens unit cell is shown in Fig. 1. The unit cell is composed of a dielectric substrate in the middle layer and asymmetric metal elements on both sides, with the period length of $P = 3.7$ mm. The dielectric substrate is F4B with the permittivity $\varepsilon = 2.2$ and thickness $h = 1.2$ mm. The metal elements on the same side are composed of U-shaped and arc-shaped structures. The horizontal metal strip is $l_1 = 3.5$ mm, and the radius of arc-shaped structure is $r = 1.55$ mm. The width of all metal strips is $d = 0.2$ mm. On the basis of ensuring the transmission amplitude, the phase coverage of $2\pi$ is achieved through the metal strip size $l_2$ and metal arc angle $\theta$.

The relationship between the electromagnetic resonance of the Huygens unit cell and the transmission amplitude is shown in Fig. 2(a). It shows that the Huygens unit cell exhibits a broadband transmission spectrum, with two near-unity transmission peaks at frequencies of 32.75 and 37.45 GHz. At both frequencies, the imaginary part of $Y_{es}\eta$ is equal to that of $Z_{ms}/\eta$, and both their real parts are near zero. The balance conditions of the generated electric and magnetic currents are satisfied, resulting in electromagnetic resonance, which causes the two transmission amplitudes to reach the peak. The principle can be analyzed by the surface currents distribution. The surface currents at the resonance frequency of 32.75 GHz are shown in Fig. 2(b). In the overlapping area of the upper and lower metal

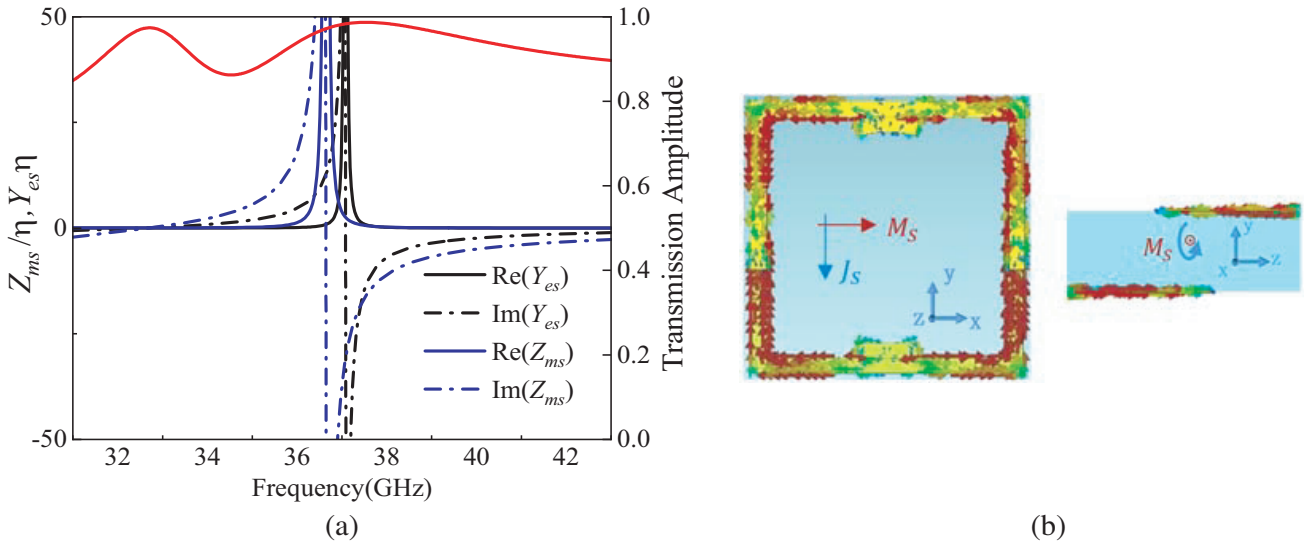


**Figure 2.** (a) The relationship between the resonance frequency and the transmission amplitude. (b) The surface currents at the resonance frequency of 32.75 GHz.

arms, the surface currents in opposite directions form a circulating current on the $yoz$ plane, thereby inducing a virtual magnetic current along the $x$-axis orthogonal to the electric currents, which excites the electromagnetic resonance.

According to the simulation, electromagnetic resonance can be obtained by adjusting the dimensions of unit cell. This mechanism enables the control of both electric and magnetic resonances, enabling complete phase coverage. Therefore, a database mapping transmission amplitude and transmission phase as a function of $l_2$ and $\theta$ is established by full-wave simulations. The value of $l_2$ increases linearly from 0.8 to 1.95 mm, and the value of $\theta$ increases linearly from 0° to 175°. Fig. 3(a) displays a database mapping transmission amplitude, with the transmission amplitude reaching 0.8 on the dotted line. Fig. 3(b) displays a database mapping transmission phase, which demonstrates that complete phase coverage is achieved by designing Huygens unit cells.

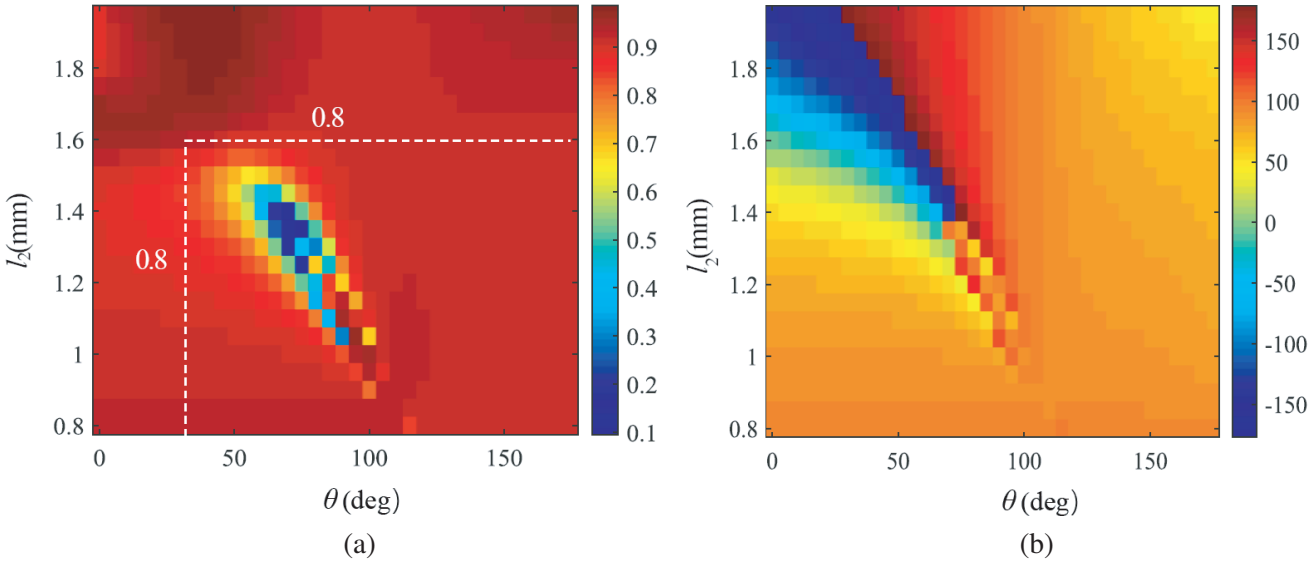


**Figure 3.** (a) Color map of the database relating $l_2$ and $\theta$ with transmission amplitude. (b) Color map of the database relating $l_2$ and $\theta$ with transmission phase.

Based on the transmission amplitude greater than 0.8, a $2\pi$ phase coverage is achieved by changing the metal element parameters of the unit cell. The upper and lower metal arms of the unit cell do not overlap when the size $l_2$ is increased from 1.2 mm to 1.55 mm, but the generated surface electric and magnetic currents reach the equilibrium condition of electromagnetic resonance. The upper and lower metal arms begin to overlap when $l_2 > 1.55$ mm. The strong magnetic currents are generated in the overlapping area, which are strong enough to balance the electric currents, excite Huygens resonance, and form two transmission amplitude peaks. However, the trough formed between the transmission peaks is less than 0.8 when $l_2 > 1.95$ mm. Considering comprehensively, under the condition that the transmission amplitude is greater than 0.8, the adjustment range of $l_2$ is from 0.8 to 1.95 mm. The phase shifts of 30.5 GHz, 37 GHz, and 43.5 GHz are shown in Fig. 4(a). Only changing the metal strip $l_2$ cannot achieve the phase coverage of $2\pi$. Embedding an arc-shaped metal element at the bottom of the U-shaped metal element can reduce the resonant frequency by increasing the electric size. The angle $\theta$ of the arc-shaped element increases from 0° to 175°, and the phase shifts at 30.5 GHz, 37 GHz, and 43.5 GHz are shown in Fig. 4(b). A complete $2\pi$ phase coverage is achieved by changing the metal strip $l_2$ and angle $\theta$ of the arc-shaped element, as shown in Table 1. Furthermore, different from a plane wave incidence, the actual measured metasurface is fed by a horn whose radiation features a spherical wave front, and the performance of the unit cell thus needs to be analyzed under oblique incidence. As shown in Fig. 5, for oblique incidence, the maximum incidence angle $\theta_i$ with transmission amplitude above 0.8 reaches 15°, and the transmission phase is consistent with the normal incidence.

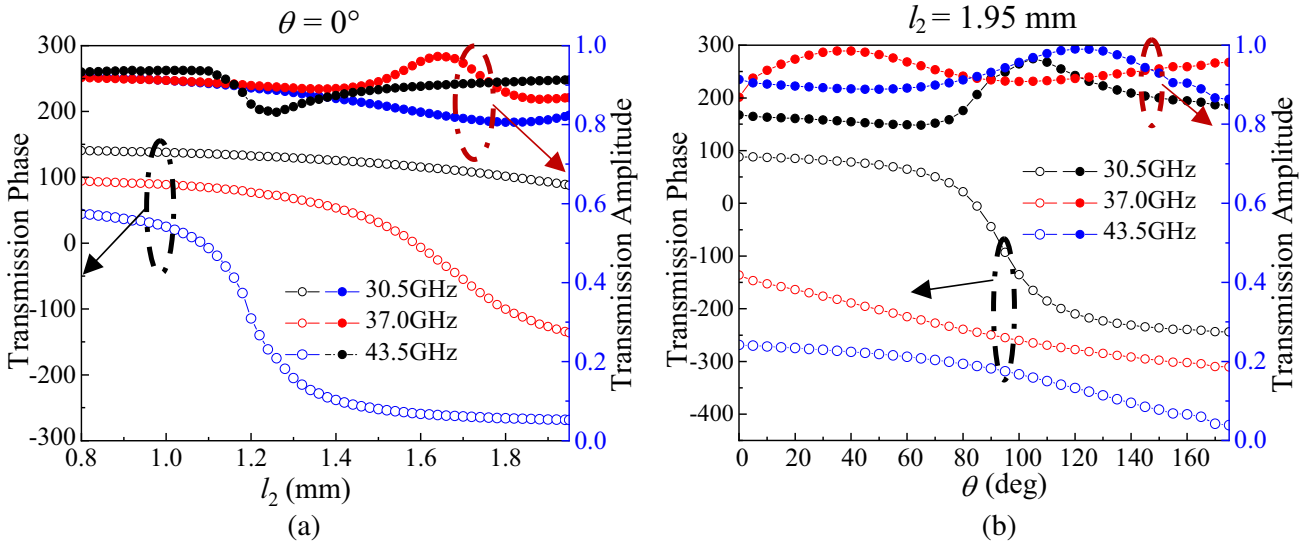


**Figure 4.** (a) Transmission amplitude and phase with different $l_2$. (b) Transmission amplitude and phase with different $\theta$.

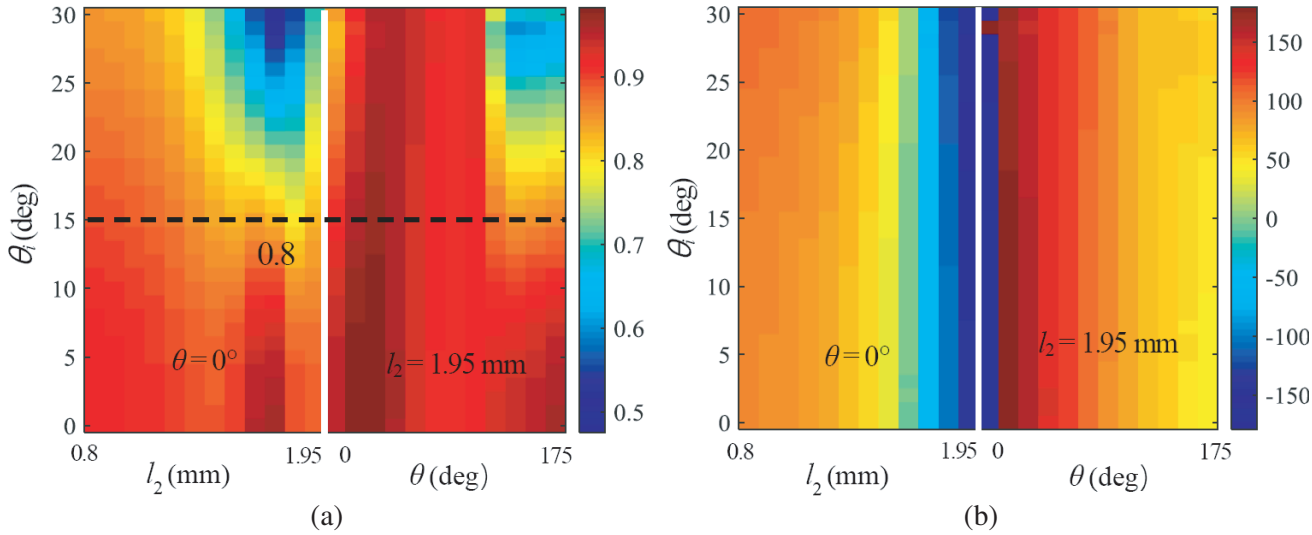


**Figure 5.** (a) Color map of the database relating $\theta_i$ with transmission amplitude. (b) Color map of the database relating $\theta_i$ with transmission phase.

## 3. MULTI-FOCUS MATESURFACE

Multi-focus can be achieved by modulating phase distribution of the metasurface based on the holographic theory [21], as shown in Fig. 6. By introducing the required phase change to the transmitted wave using the proposed unit cell, the incident wave can be focused to a specified position. In order to realize a multi-focus metasurface, one or more preset foci are regarded as virtual point sources, which radiate spherical wave deemed as the object wave, and the plane wave incident on the metasurface is deemed as the reference wave. Then the electric field generated by each virtual source can be superimposed to obtain the virtual electric field distribution $E_{Fcous}(x_i, y_i, 0)$. Here the electromagnetic

**Table 1.** Total phase shift with the different $l_2$ and $\theta$.

| Freq. (GHz) | Mini Transmission Amplitude | $l_2$ Phase Shift | $\theta$ Phase Shift | Total Phase Shift |
|---|---|---|---|---|
| 31 | 0.81 | 55° | 328° | 383° |
| 33 | 0.84 | 101° | 293° | 394° |
| 35 | 0.83 | 174° | 218° | 392° |
| 37 | 0.87 | 230° | 170° | 400° |
| 39 | 0.91 | 274° | 142° | 416° |
| 41 | 0.9 | 299° | 136° | 435° |

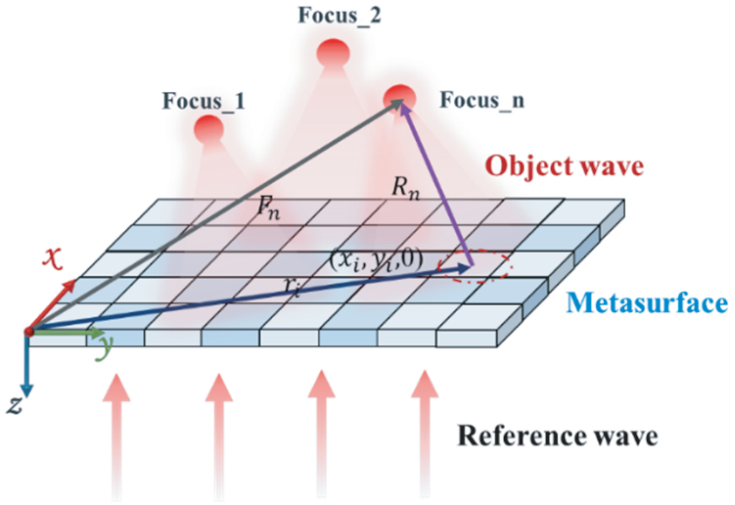


**Figure 6.** Schematic diagram of multi-focus metasurface.

field propagation from each virtual point source is described by Green function.

$$E_{Fcous}(x_i, y_i, 0) = \sum_{n=1}^{N} [w_{Fn} \cdot G(R_n)] \tag{3}$$

$$E_{Fcous}(x_i, y_i, 0) = \sum_{n=1}^{N} \left[\frac{w_{Fn} \cdot \exp(jk_0 R_n)}{R_n}\right] = \sum_{n=1}^{N} \left[\frac{w_{Fn} \cdot \exp(jk_0 |F_n - r_i|)}{|F_n - r_i|}\right] \tag{4}$$

where $(x_i, y_i, 0)$ represents the center coordinates of the $i$-th metasurface unit cell, and $w_{Fn}$ is the weight factor of intensity of the $n$-th virtual focal point, which can directly affect the intensity distribution of reconstructed electric field. $R_n$ is the distance from the $n$-th point source to the $i$-th metasurface unit cell, and $k$ is the free space wave number. $F_n$ is the distance from the $n$-th focus to the origin, and $r_i$ is the distance from the $i$-th metasurface unit cell to the origin. $N$ is the number of focal points. Particularly, multi-focus with different spatial positions, electric field distributions, and focusing intensities can be realized according to parameters $R_n N$ and $w_{Fn}$. Then the virtual electric field is mapped onto the metasurface, and the desired phase delay at the positions of different metasurface unit cell can be calculated.

$$\varphi_{Fcous}(x_i, y_i, 0) = \text{angle} \sum_{n=1}^{N} \left[\frac{w_{Fn} \cdot \exp(jk_0 |F_n - r_i|)}{|F_n - r_i|}\right] \tag{5}$$

The reference wave is the incident plane wave. The amplitude and phase of each unit cell incident on the metasurface are constant, assuming that the phase is $\varphi_d$. According to the holographic theory, the object wave and reference wave are superimposed, and the phase distribution that needs to be compensated at the metasurface position is

$$\varphi(x_i, y_i, 0) = \varphi_d - \varphi_{Fcous}(x_i, y_i, 0) \tag{6}$$

According to the design idea of theoretical analysis, the number and positions of the foci can be designed as required. Taking double-foci as an example, the positions of two focal points are $F_1 = (-25, 0, 50)$ mm $F_2 = (25, 0, 50)$ mm. To achieve the uniform intensity ratio, the weight factors are equal. According to formula (7), we calculate the spatially accumulated phase of the electromagnetic wave from the $i$-th unit cell on the metasurface to the focus.

$$\varphi(x_i, y_i, 0) = \varphi_d - \varphi_{Fcous}(x_i, y_i, 0) = \varphi_d - \text{angle} \sum_{n=1}^{2} \left[ \frac{w_{Fn} \cdot \exp\left(jk_0 \left|F_n - r_i\right|\right)}{\left|F_n - r_i\right|} \right] \tag{7}$$

The phase information that needs to be compensated for the metasurface is calculated, as shown in Fig. 7(a), and the result of double-focus focusing at 37 GHz is simulated, as shown in Fig. 7(b). They show that by carefully designing the phase distribution, when a $y$-polarized electromagnetic wave is incident, the energy is concentrated on the $xoy$ plane with a focal length of $Z = 50$ mm. The energy of the convergence point is much higher than the energy of the incident wave, which verifies the feasibility of using the above theory to design metasurfaces. Fig. 7(b) shows that there is a small number of

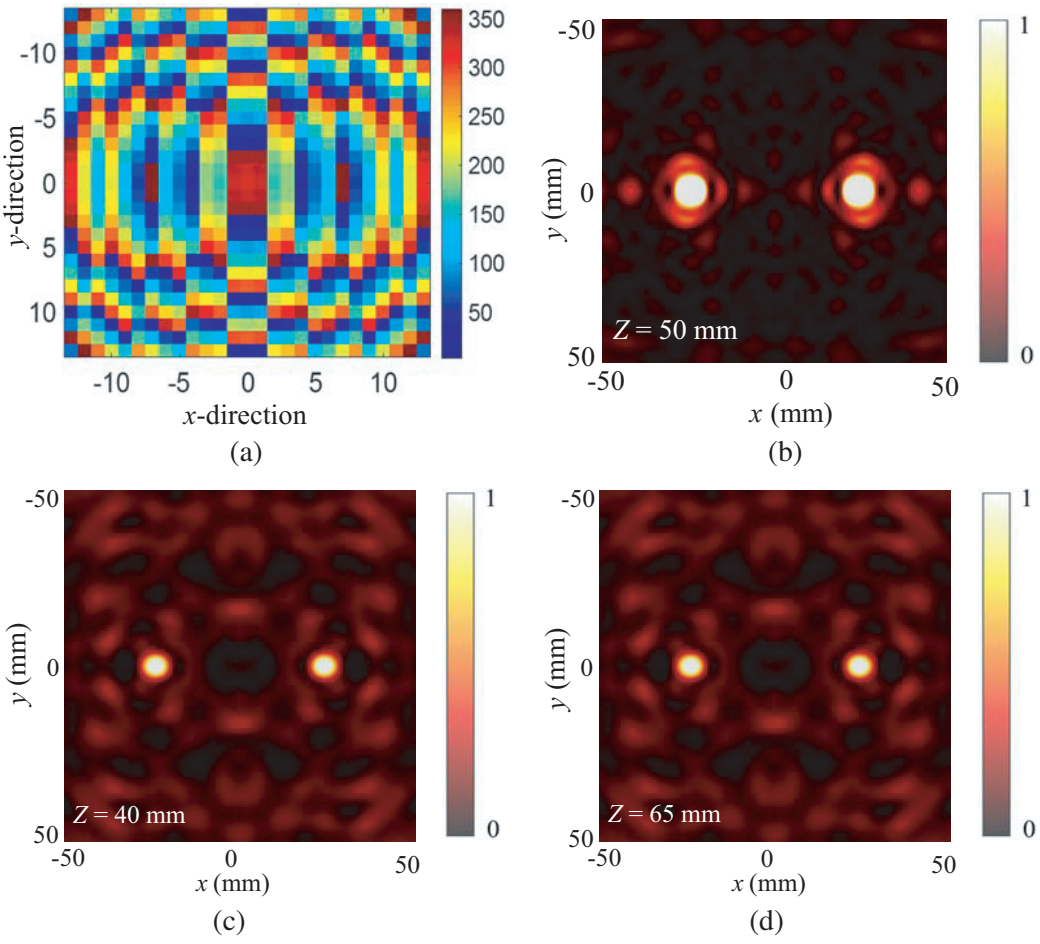


**Figure 7.** (a) Metasurface phase distribution. (b), (c) and (d) Energy distribution in the $xoy$ plane at 37 GHz, 31 GHz, 43 GHz.

diffracted fields near the two focal points. These higher order harmonic components are induced by the electromagnetic wave that propagates through the metasurface. To improve the focusing quality, some algorithms can be applied for optimization. The two focal points designed at 37 GHz can also be observed from 31 to 43 GHz, as shown in Figs. 7(c) and (d). They show that the designed metasurface has excellent broadband focusing ability, while the focusing position and quality are closely related to the operating frequency. According to formula (5), the phase compensation of the metasurface is constant, and the focal length of each focusing plane varies with the operating frequency. The relationship between the focusing position and wavelength can be derived under the paraxial approximation.

## 4. FABRICATION AND MEASUREMENT

Using planar printed circuit board technology, a metasurface array with a center frequency of $f_c = 37$ GHz and $27 \times 27$ unit cells is fabricated and measured, as shown in Figs. 8(a) and (b). The center of the horn antenna and the center of the metasurface array are kept in a horizontal line, so that the radiated electromagnetic wave is irradiated vertically on the metasurface as a plane wave, and then

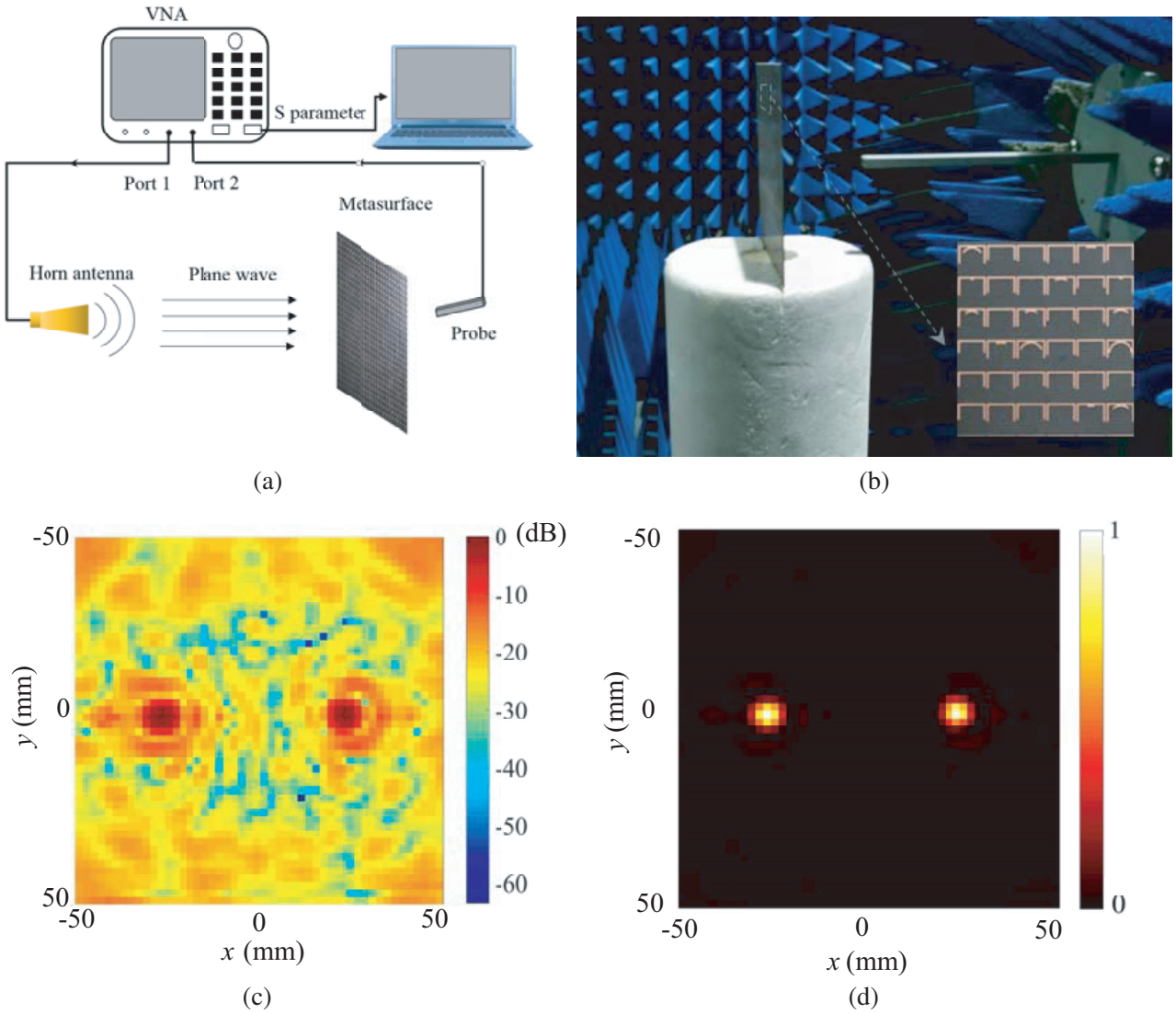


**Figure 8.** (a) Experimental setup for the measurement. (b) Measured scene. (c) Measured result at 37 GHz. (d) Normalized measured result at 37 GHz.

passes through the metasurface and is received by the probe. The measured result of the electric field of the metasurface in the $xoy$ plane at $Z = 50$ mm is shown in Fig. 8(c), and the normalized measured result is shown in Fig. 8(d). The measured results show that the metasurface can achieve a good double-focus focusing effect.

The electric field on the $x$-axis is measured by a vector network analyzer and is fitted into a normalized electric field distribution curve, as shown in Fig. 9(a). The dotted line is the actual measured result, and the solid line is the simulation result. The simulated and measured results are basically the same. Due to the limitation of the measured environment and other factors, the focus position obtained in the measured result is horizontally shifted by 2 mm. The focusing efficiency is shown in Fig. 9(b). Here, the focusing efficiency is defined as the ratio of the energy of the two focal points (the energy between the first dark ring) and the plane energy at the same position when there is no metasurface. At 37 GHz, the simulated focusing efficiency is the highest, reaching 43.78%. The highest focusing efficiency obtained in the measured result is also at 37 GHz, which is 39.50%. The relative bandwidth at which the focusing efficiency reaches 20% is about 20.3%. The measured efficiency is slightly lower than the simulated one, which may be caused by the coupling between the unit cells, compensated phase error, machining imperfection, and measurement error. In addition, the slight intensity variation between the two focal points in Fig. 8(c) mainly comes from the slight off-axis deviation of non-planar wavefronts of the incident field distribution from the feeding horn antenna across the metasurface, compared to normally incident ideal planar wavefronts considered in simulations. The metasurface based on the incidence of $y$-polarized electromagnetic wave can achieve energy convergence in a wide frequency range of $31 \sim 43$ GHz. Compared with multi-layer metasurfaces, the proposed metasurface has a low-profile characteristic with a thickness of 1.2 mm, a broadband characteristic with an absolute bandwidth of 12 GHz, and a high focusing efficiency of over 40%.

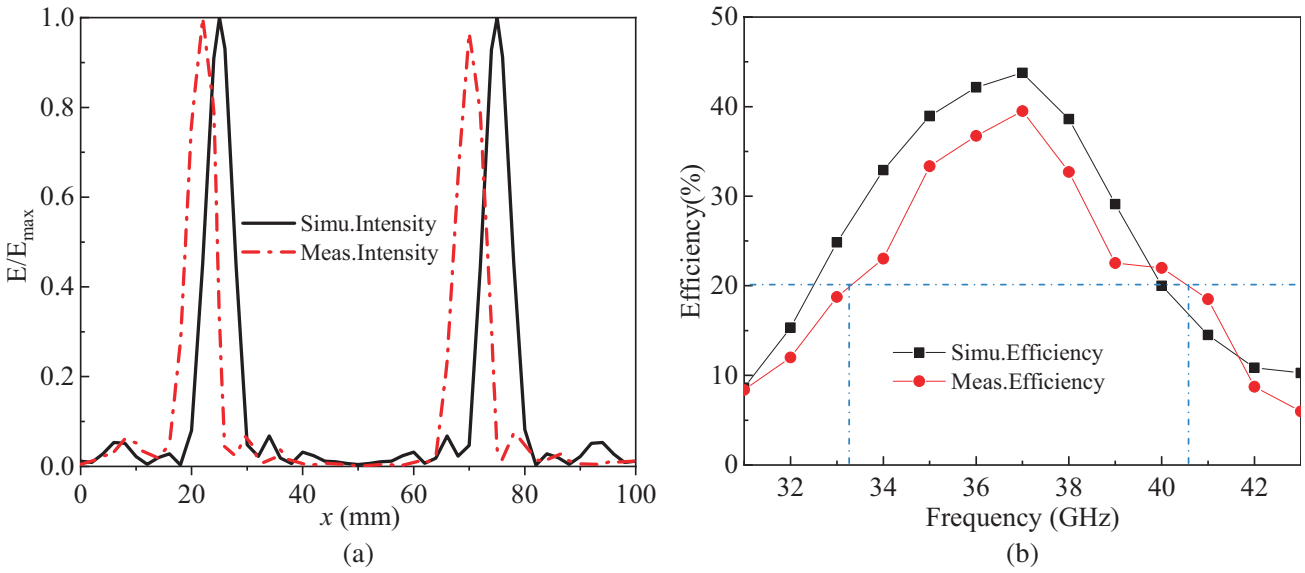


**Figure 9.** (a) The measured and simulated normalized electric field. (b) The measured and simulated focusing efficiency.

Table 2 compares the important performance indicators of the proposed metasurface with the six reported metasurfaces. The single-layer design with vias [22], double-layer type [26, 28], and triple-layer type [27] fulfill high efficiency and full phase shift at the price of complex structure and expensive fabrication. We use a single-layer design without vias to achieve a full phase shift of $2\pi$ and high transmission amplitude, which effectively improves the focusing efficiency of the metasurface. By comparison, our design exhibits the unique advantage that the excellent performances of high efficiency over a broadband width are achieved in a very simplified structure. The proposed metasurface is vialess

**Table 2.** Comparison of the proposed metasurface with referenced designs.

| Ref. | Freq. (GHz) | Max. Transmission Loss | Number Layers & Style | Phase Shift | Efficiency |
|---|---|---|---|---|---|
| [22] | 6.9 | / | 1 | 360° | 36% |
| [25] | 10 | −3 dB | 2 | 353° | 36% |
| [26] | 11.7 | about −2.15 dB | 3 | 360° | 62% |
| [27] | 10 | −3 dB | 2 | 353° | 36% |
| [28] | 10 | −1.1 dB | 1 & vias | 300° | 6.88% |
| [24] | 10 | −1.67 dB | 1 | 360 | 47% |
| Ours | 37 | −1.2 dB (0.87) | 1 | > 360° | 39.5% |

and can be printed on both sides of one PCB board, which makes the fabrication much easier with lower cost. In addition, compared with references [22, 24], the proposed Huygens unit cell does not build a magnetic dipole separately, which eliminates the need for magnetic components in the physical structure and makes the metasurface more compact.

## 5. CONCLUSION

In conclusion, a single layer Huygens unit cell based on induced magnetism is proposed to design a metasurface with multi-focus focusing characteristics. The induced magnetism in the Huygens unit cell proposed originates from the circulating current generated by two asymmetric electric dipole elements, without separate magnetic dipole component. The physical structure eliminates the need for separate magnetic elements, making the metasurface more compact and easier to manufacture. In addition, parametric tuning of Huygens unit cell provides $2\pi$ phase coverage and high transmission amplitude. On this basis, a multi-focus Huygens metasurface is proposed. Arbitrary focusing can be achieved at millimeter wave range considering the factors of focal number, location, and intensity ratio. To demonstrate it, the electric field distribution of the double-focus metasurface is measured, which is consistent with the simulations. They show that when a $y$-polarized electromagnetic wave is incident, the energy is concentrated in a preset plane by carefully designing the phase distribution. The energy of the convergence point is much higher than the energy of the incident wave, which verifies the feasibility of using holographic theory to design metasurfaces. The proposed multi-focus Huygens metasurface has potential applications in antennas and imaging systems. Furthermore, the proposed Huygens metasurface design method with multi-focus function can also be applied to other frequency ranges.

## ACKNOWLEDGMENT

This work was supported in part by the Natural Science Foundation of Chongqing (cstc2018jcyjAX0508), in part by the Research Program of Chongqing Municipal Education Commission (KJQN201800639).

## REFERENCES

1. Marcin, K., "Real-time concealed object detection and recognition in passive imaging at 250 GHz," *Appl. Opt.*, Vol. 58, 3134–3140, 2019.
2. Li, H. S., X. W. Zhang, X. Q. Zhang, and L. P. Lu, "Design of photoelectric detection sensor incorporated with meso-lens array and its detection screen performance analysis," *IEEE Sens. J.*, Vol. 21, 1444–1452, 2021.

3. Cu-Nguyen, P. H., G. Adrian, F. Patrik, S. Andreas, S. Stefan, and Z. Hans, "An imaging spectrometer employing tunable hyperchromatic microlenses," *Light: Sci. Appl.*, Vol. 5, e16058, 2016.
4. Yuichi, K., M. Daichi, and S. Shunichi, "Superresolution imaging via superoscillation focusing of a radially polarized beam," *Optica.*, Vol. 5, 86–92, 2018.
5. Choi, W. C., S. Lim, and Y. J. Yoon, "Evaluation of transmit-array lens antenna for deep-seated hyperthermia tumor treatment," *IEEE Antennas Wirel. Propag. Lett.*, Vol. 19, 866–870, 2020.
6. Liao, C. S., P. Wang, C. Y. Huang, P. Lin, G. Eakins, R. T. Bentley, R. G. Liang, and J. X. Cheng, "In vivo and in situ spectroscopic imaging by a handheld stimulated raman scattering microscope," *ACS Photonics*, Vol. 5, 947–954, 2018.
7. Yang, L., Y. Zeng, and R. Zhang, "Channel estimation for millimeter-wave MIMO communications with lens antenna arrays," *IEEE Trans. Veh. Technol.*, Vol. 67, 3239–3251, 2018.
8. Su, Y. Y. and Z. N. Chen, "A radial transformation-optics mapping for flat ultra-wide-angle dual-polarized stacked GRIN MTM luneburg lens antenna," *IEEE Trans. Antennas Propag.*, Vol. 67, 2961–2970, 2019.
9. Hsiao, H. H., C. H. Chu, and D. P. Tsai, "Fundamentals and applications of metasurfaces," *Small Methods*, Vol. 1, 1600064, 2017.
10. Wu, R. Y., L. Bao, L. W. Wu, Z. X. Wang, Q. Ma, J. W. Wu, G. D. Bai, V. Galdi, and T. J. Cui, "Independent control of copolarized amplitude and phase responses via anisotropic metasurfaces," *Adv. Opt.*, Vol. 8, 1902126, 2020.
11. Bao, L., R. Y. Wu, X. J. Fu, Q. Ma, G. D. Bai, J. Mu, R. Z. Jiang, and T. J. Cui, "Multi-beam forming and controls by metasurface with phase and amplitude modulations," *IEEE Trans. Antenn. Propag.*, Vol. 66, 6680–6685, 2019.
12. Mueller, J. P. B., N. A. Rubin, R. C. Devlin, B. Groever, and F. Capasso, "Metasurface polarization optics: Independent phase control of arbitrary orthogonal states of polarization," *Phys. Rev. Lett.*, Vol. 118, 113901, 2017.
13. Arbabi, A., Y. Horie, M. Bagheri, and A. Faraon, "Dielectric metasurfaces for complete control of phase and polarization with subwavelength spatial resolution and high transmission," *Nat. Nanotechnol.*, Vol. 10, 937–943, 2015.
14. Liu, W. W., S. Q. Chen, Z. C. Li, H. Cheng, P. Yu, J. X. Li, and J. G. Tian, "Realization of broadband cross-polarization conversion in transmission mode in the terahertz region using a single-layer metasurface," *Opt. Lett.*, Vol. 40, 3185–3188, 2015.
15. Zou, M., M. Su, and H. Yu, "Ultra-broadband and wide-angle terahertz polarization converter based on symmetrical anchor-shaped metamaterial," *Opt. Mater.*, Vol. 107, 110062, 2020.
16. Cai, T., G. M. Wang, S. W. Tang, H. X. Xu, J. W. Duan, H. J. Guo, F. X. Guan, S. L. Sun, Q. He, and L. Zhou, "High-efficiency and full-space manipulation of electromagnetic wave fronts with metasurfaces," *Phys. Rev. Appl.*, Vol. 8, 034033, 2017.
17. Cheng, K. Y., Z. Y. Wei, Y. C. Fan, X. M. Zhang, C. Wu, and H. Q. Li, "Realizing broadband transparency via manipulating the hybrid coupling modes in metasurfaces for high-efficiency metalens," *Adv. Opt. Mater.*, Vol. 7, 1900016, 2019.
18. Pfeiffer, C. and A. Grbic, "Metamaterial Huygens' surfaces: Tailoring wave fronts with reflectionless sheets," *Phys. Rev. Lett.*, Vol. 110, 197401, 2013.
19. Xu, H. X., G. W. Hu, L. Han, M. H. Jiang, Y. J. Huang, Y. Li, X. M. Yang, X. H. Ling, L. Z. Chen, J. L. Zhao, and C. W. Qiu, "Chirality-assisted high-efficiency metasurfaces with independent control of phase, amplitude, and polarization," *Adv. Opt. Mater.*, Vol. 7, 1801479, 2019.
20. Jia, S. L., X. Wan, X. J. Fu, Y. J. Zhao, and T. J. Cui, "Low-reflection beam refractions by ultrathin huygens metasurface," *AIP Adv.*, Vol. 5, 4773–4776, 2015.
21. Wang, Z. C., X. M. Ding, K. Zhang, and Q. Wu, "Spacial energy distribution manipulation with multi-focus Huygens metamirror," *Sci. Rep.*, Vol. 7, 9081, 2017.

22. Chen, K., Y. J. Feng, F. Monticone, J. M. Zhao, B. Zhu, T. Jiang, L. Zhang, Y. Kim, X. M. Ding, S. Zhang, A. Alu, and C. W. Qiu, "A reconfigurable active Huygens' metalens," *Adv. Mater.*, Vol. 29, 1606422, 2017.
23. Abdo-Sanchez, E., M. Chen, A. Epstein, and G. V. Eleftheriades, "A leaky-wave antenna with controlled radiation using a bianisotropic Huygens' metasurface," *IEEE Trans. Antennas Propag.*, Vol. 67, 108–120, 2019.
24. Song, L. Z., P. Y. Qin, and Y. J. Guo, "A high-efficiency conformal transmitarray antenna employing dual-layer ultrathin Huygens element," *IEEE Trans. Antennas Propag.*, Vol. 69, 848–858, 2021.
25. Tian, C., Y. C. Jiao, and G. Zhao, "Circularly polarized transmitarray antenna using low-profile dual-linearly polarized elements," *IEEE Trans. Antennas Propag.*, Vol. 16, 465–468, 2017.
26. Hsu, C. Y., L. T. Hwang, T. S. Horng, S. M. Wang, F. S. Chang, and C. N. Dorny, "Transmitarray design with enhanced aperture efficiency using small frequency selective surface cells and discrete Jones matrix analysis," *IEEE Trans. Antennas Propag.*, Vol. 66, 3983–3994, 2018.
27. Yi, X., T. Su, X. Li, B. Wu, and L. Yang, "A double-layer wideband transmitarray antenna using two degrees of freedom elements around 20 GHz," *IEEE Trans. Antennas Propag.*, Vol. 67, 2798–2802, 2019.
28. Islam, K. M. R. and S. Choi, "Compact double-layer FR4-based focusing lens using high-efficiency Huygens' metasurface unit cells," *Sensors*, Vol. 20, 6142, 2020.